

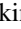
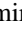






Electron-nuclei interaction in the X valley of (In,Al)As/AlAs quantum dots

M. S. Kuznetsova ¹, J. Rautert ², K. V. Kavokin ¹, D. S. Smirnov ³, D. R. Yakovlev ^{2,3}, A. K. Bakarov ⁴,
A. K. Gutakovskii,⁴ T. S. Shamirzaev ^{4,5} and M. Bayer ^{2,3}

¹*Spin Optics Laboratory, Saint Petersburg State University, 198504 St. Petersburg, Russia*

²*Experimentelle Physik 2, Technische Universität Dortmund, D-44221 Dortmund, Germany*

³*Ioffe Institute, Russian Academy of Sciences, 194021 St. Petersburg, Russia*

⁴*Rzhanov Institute of Semiconductor Physics, Siberian Branch of the Russian Academy of Sciences, 630090 Novosibirsk, Russia*

⁵*Ural Federal University, 620002 Yekaterinburg, Russia*



(Received 14 October 2019; revised manuscript received 16 December 2019; accepted 22 January 2020; published 11 February 2020)

The electron-nuclei hyperfine interaction of electrons in indirect band gap (In,Al)As/AlAs quantum dots with type-I band alignment has been experimentally studied by measuring the polarization degree of the photoluminescence in a transverse magnetic field (Hanle effect) and the polarization recovery in a longitudinal magnetic field. The different symmetries of the X valley electron Bloch amplitudes at the As, In, and Al nuclei strongly affect the hyperfine interaction. The hyperfine constants corresponding to these nuclei have been determined.

DOI: [10.1103/PhysRevB.101.075412](https://doi.org/10.1103/PhysRevB.101.075412)

I. INTRODUCTION

Active manipulation of the spin degrees of freedom in solid-state systems is attractive for the development of future spintronics and quantum devices for storing and processing information [1]. Heterostructures on the basis of group-III-V compound semiconductors are of particular interest since they may benefit from well-developed epitaxial technologies and possibilities of single-photon addressing for precise data writing and reading [2,3]. However, one of the hard challenges on the way to constructing such spintronic devices is the fast decoherence of electron spins due to their interaction with the dense nuclear spin environment [4–6]. Due to the s type character of the electron Bloch wave function, its hyperfine interaction is described by a single hyperfine constant A , proportional to the electron density at the nucleus [6,7]. Valence-band holes are more robust against spin decoherence owing to their weaker hyperfine coupling compared to electrons [5]. Since this robustness is a result of the different symmetries of the Bloch amplitudes [8], it is interesting to study the hyperfine interaction for electrons in indirect gap minima of the Brillouin zone, where the wave functions are not of a pure s type. Convenient objects for studying the hyperfine interaction of such electrons are indirect band gap quantum wells (QWs) and quantum dots (QDs) [9]. In the scarce experimental studies of the hyperfine interaction of electrons in AlAs QWs published so far, an electron spin resonance technique was used [10], which is difficult to apply to QDs.

A useful method for creating spin polarization of electrons that interact with nuclei is optical orientation [11]. However, the weak coupling of electronic states with light hampers using this technique for indirect band gap heterostructures. Recently, we demonstrated that effective optical orientation can be reached in the (In,Al)As/AlAs QD system [12].

In these (In,Al)As/AlAs QDs the electron ground state shifts from the Γ to the X valley with decreasing dot diameter,

while the heavy-hole (hh) ground state remains at the Γ point. This corresponds to a change from a direct to an indirect band gap in momentum space, while the type-I band alignment is preserved [13,14]: the lowest electron level in small-diameter QDs with strong quantum confinement along the growth direction belongs to the X valley. With increasing dot diameter, the Γ valley level shifts to lower energies more rapidly than the X level due to the smaller effective mass of the Γ valley electrons [15]. The complicated energy spectrum of indirect band gap (In,Al)As/AlAs QDs allows one to populate the indirect electron states in a quasiresonant optical excitation regime [12].

In this paper, the electron-nuclear hyperfine interaction in (In,Al)As/AlAs QDs with type-I band alignment and indirect band gap structure is studied. The circular polarization of the photoluminescence excited using optical orientation with a transverse (Hanle effect) or a longitudinal (polarization recovery effect) magnetic field applied is measured. We demonstrate that at low temperatures the half width at half maximum (HWF) of the Hanle curve does not depend on the spin relaxation time. Instead, it is determined by the hyperfine interaction with the nuclear field fluctuations. We develop a microscopic theory of the hyperfine interaction for electrons in the conduction band X valleys using a symmetry analysis and density functional theory (DFT) calculations. The constants of hyperfine interaction for these X valley electrons with the As, In, and Al nuclei are determined.

II. EXPERIMENTAL DETAILS

The studied self-assembled (In,Al)As QDs, embedded in an AlAs matrix, were grown by molecular-beam epitaxy on a semi-insulating (001)-oriented GaAs substrate. The structure contained one QD sheet sandwiched between 70-nm-thick AlAs layers grown on top of a 400-nm-thick GaAs buffer

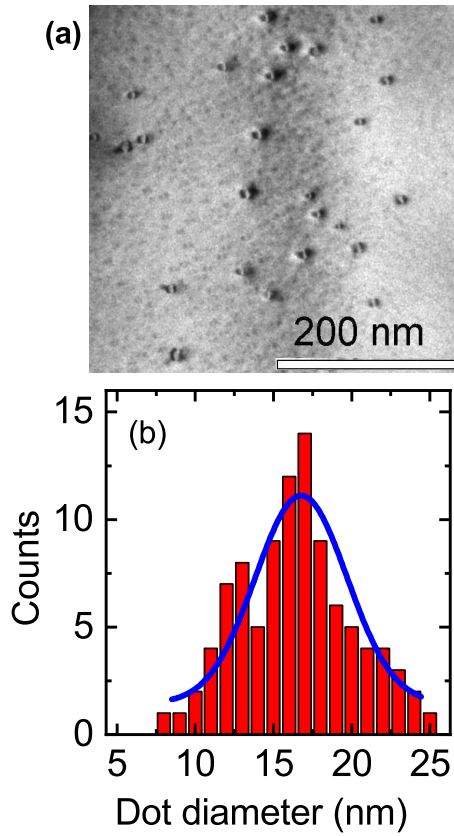


FIG. 1. (a) TEM plane-view image and (b) the corresponding histogram of the QD-diameter distribution for the studied (In,Al)As/AlAs QDs. The size dispersion fitted by a Gaussian distribution is shown by the blue line. The average diameter is $D_{av} = 16.7$ nm.

layer. The nominal amount of deposited InAs was about 2.7 monolayers. A 20-nm-thick GaAs cap layer protects the top AlAs barrier from oxidation. In order to increase the light emission output from the QDs, the sample was covered by a SiO₂ antireflection coating layer with a thickness of 150 nm. The growth axis coincides with the crystallographic (001) direction and is taken as the z axis. Note that the band gap energy of the GaAs substrate is 1.52 eV, while that of the AlAs barrier is 2.30 eV [16]. Further growth details are given in Ref. [13].

The QD size and density were studied by transmission electron microscopy (TEM) using a JEM-4000EX system operated at an acceleration voltage of 200 keV. A TEM plane-view image and the corresponding histogram of the QD-diameter distribution are shown in Fig. 1. The density of lens-shaped QDs is about $1.2 \times 10^{10} \text{ cm}^{-2}$. The average dot diameter is $D_{av} = 16.7$ nm, while at the upper and lower wings of the distribution function the half maximum corresponds to $D_L = 20.5$ nm and $D_S = 13$ nm, respectively. The aspect ratio of the diameter to height of the QDs is 3:1, and the average volume of a QD is $V_{av} = 1.18 \times 10^3 \text{ nm}^3$. The accuracy of the QD size determination does not exceed 25% [14]. The span of the QD size distribution is $S_D = 100 \times (D_L - D_S)/D_{av} \approx 50\%$. Since the shape of the photoluminescence (PL) emission reflects the distribution of QD sizes and chemical composition practically does not change with quantum dot diameter,

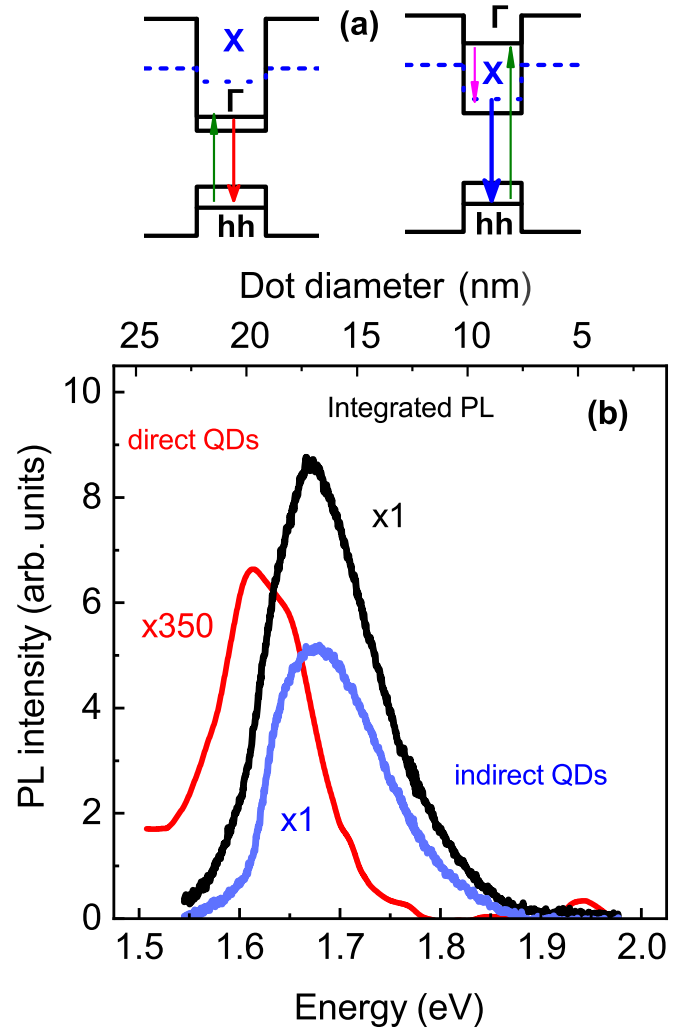


FIG. 2. (a) Band diagrams of (In,Al)As/AlAs QDs with different band structures. Vertical arrows illustrate excitation, energy relaxation, and recombination processes of electrons in QDs under selective excitation. (b) Photoluminescence spectra of (In,Al)As/AlAs QDs measured under nonresonant excitation: time integrated (black line) as well as time resolved for $t_{\text{delay}} = 0$ ns and $t_{\text{gate}} = 10$ ns (red line) and for $t_{\text{delay}} = 500$ ns and $t_{\text{gate}} = 450 \mu\text{s}$ (blue line). $T = 1.8$ K. QD diameters corresponding to PL emission energies are given on the top axis.

as shown in Ref. [13], we can establish the relation between the parameters characterizing the spectra and the geometric quantities. For the studied structure, the average QD composition is determined to be In_{0.64}Al_{0.36}As. The dispersion of size, shape, and composition within the QD ensemble results in the simultaneous presence of (In,Al)As/AlAs QDs with type-I band alignment and with the lowest conduction-band states at either the Γ or X_{XY} minima of the (In,Al)As conduction band [14] [see Fig. 2(a)].

Weak magnetic fields (in the millitesla range) were generated by an electromagnet with accuracy better than 0.01 mT. The magnetic field was applied either parallel to the structure growth axis ($\mathbf{B} \parallel z$) in Faraday geometry or perpendicular to it ($\mathbf{B} \perp z$) in Voigt geometry.

The photoluminescence was excited either nonresonantly with the photon energy of the laser exceeding considerably

the emission energies of the QD ensemble or selectively with the laser energy tuned resonantly within the inhomogeneously broadened exciton emission band of the QDs. The nonresonant excitation was provided by the third harmonic of a Q -switched Nd:YVO₄ pulsed laser with photon energy of 3.49 eV, pulse duration of 5 ns, and repetition rate of 2 kHz [17]. The excitation density was kept below 100 nJ/cm². For selective excitation in the energy range of 1.50–1.79 eV, a tunable continuous-wave Ti:sapphire laser was used.

The PL emission was dispersed by a 0.5-m monochromator. For the time-integrated measurements under nonresonant excitation, the PL was detected by a liquid-nitrogen-cooled charge-coupled-device (CCD) camera. For the time-resolved PL at nonresonant excitation we used a gated CCD camera synchronized with the laser via an external trigger signal. Here, t_{delay} is the time between the laser pulse and the start of the exposure. It could be varied from 0 ns up to 500 μ s. The duration of the exposure, the gate window t_{gate} , could be extended from 1 ns to 500 μ s. Signal intensity and time resolution depend on the choice of t_{delay} and t_{gate} . The highest resolution of the detection system was 1 ns.

We investigate the electron spin dynamics by measuring the polarization degree of PL in transverse magnetic field (Hanle effect) and restoration of the polarization in longitudinal magnetic field [polarization recovery curve (PRC)]. The PL was detected with a silicon avalanche photodiode. For the optical orientation measurements, circular polarizers (Glan-Thompson prism and a quarter-wave plate) were installed in both the excitation and detection optical pathways. The circular polarization degree was determined as $\rho_c = (I^{++} - I^{--}) / (I^{++} + I^{--})$, where I^{++} (I^{--}) stands for the PL intensity in co- (cross-) circular polarization relative to that of excitation.

Time-resolved photoluminescence under nonresonant excitation

Photoluminescence spectra of an (In,Al)As/AIAs QD ensemble measured under nonresonant excitation are shown in Fig. 2(b). The time-integrated spectrum (black line) has a maximum at 1.67 eV and extends from 1.55 up to 1.9 eV, having a full width at half maximum (FWHM) of 140 meV. Since the shape of the PL emission reflects the distribution of QD sizes, we can establish the relation between the parameters characterizing the spectra and the geometric quantities. The top axis in Fig. 2(b) gives the QD diameters that correspond to particular PL emission energies. The large width of the emission band is due to the dispersion of the QD parameters since the exciton energy depends on the QD size, shape, and composition [13]. The PL band is contributed by the emission of direct and indirect QDs, which becomes evident from time-resolved PL spectra [12]. As measured immediately after the laser pulse ($t_{\text{delay}} = 0$ ns and $t_{\text{gate}} = 10$ ns) excitation, the PL band has a maximum at 1.61 eV and a FWHM of 80 meV (red line). For longer delays ($t_{\text{delay}} = 500$ ns and $t_{\text{gate}} = 450$ μ s) the emission maximum shifts to 1.67 eV, and the line broadens up to 130 meV (blue line), similar to the time-integrated PL spectrum. The low intensity of PL of the direct band gap QDs is a result of small concentration of big-size QDs in the ensemble.

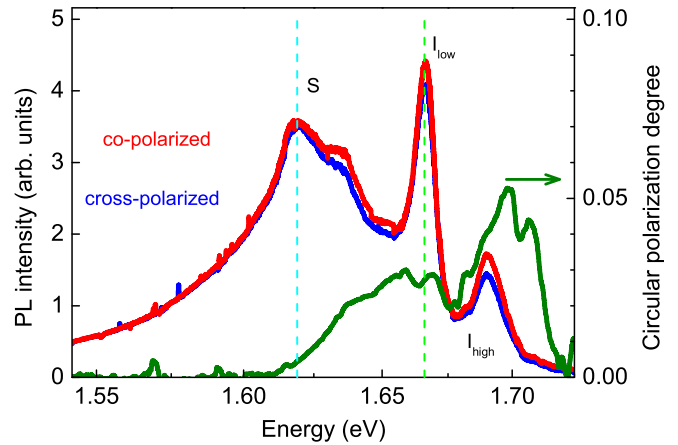


FIG. 3. PL spectra measured for σ^+ excitation at $E_{\text{exc}} = 1.727$ eV using co- and cross-polarized detection as well as the corresponding circular polarization degree. $T = 1.8$ K. Crossing energies of the PL lines from direct and indirect QDs are $E_{\Gamma X}^{\text{low}} = 1.619$ eV and $E_{\Gamma X}^{\text{high}} = 1.666$ eV, as marked by the vertical dashed lines.

The strong modification of the time-resolved spectra with time delay is a result of very different exciton recombination dynamics in direct and indirect QDs [14,17]. In indirect band gap materials, the momentum conservation law suppresses radiative recombination of electrons and holes separated in the momentum space. The radiation becomes possible due to mixing of states of different valleys of the conduction band (such as the Γ and X valleys [18]). In ideal bulk semiconductors the electron states from the Γ and X valleys do not mix with each other. However, $\Gamma - X$ mixing does take place in low-dimensional heterostructures due to scattering of the electron at the interfaces. In (In,Al)As/AIAs QDs the lowest electronic level is located at the X_{XY} minimum of the conduction band, independent of the composition [13]. Thus $\Gamma - X_{XY}$ mixing can be induced only by violation of the translational symmetry in the XY plane, which results in a very long exciton recombination time, reaching hundreds of microseconds [17]. We demonstrated recently that after photoexcitation in the AIAs barriers electrons and holes are captured in the QDs within several picoseconds, and the capture probability does not depend on the QD size and composition [19]. Therefore, all QDs in the ensemble (direct and indirect) become equally populated shortly after the excitation pulse. The exciton recombination dynamics is fast for direct QDs emitting mainly in the spectral range of 1.50–1.73 eV. On the other hand, the dynamics is slow for the indirect QDs emitting in the 1.55–1.90 eV range. The emission bands of the direct and indirect QDs overlap in the range of 1.55–1.73 eV.

In order to distinguish between direct and indirect band gap QDs within an inhomogeneously broadened PL line, we use selective excitation [12]. PL spectra measured for excitation at $E_{\text{exc}} = 1.727$ eV are shown in Fig. 3. They comprise several lines. As we showed in Ref. [12] the lines marked I_{low} and I_{high} are provided by exciton recombination in the indirect QDs, while line S arises from a transition in QDs with Γ - X mixing of the electron states. Tuning the excitation energy in the range of $E_{\text{exc}} = 1.56$ –1.79 eV allows us to selectively excite different subensembles of QDs. The energies of different PL lines as functions of E_{exc} are presented in Fig. 4. One can

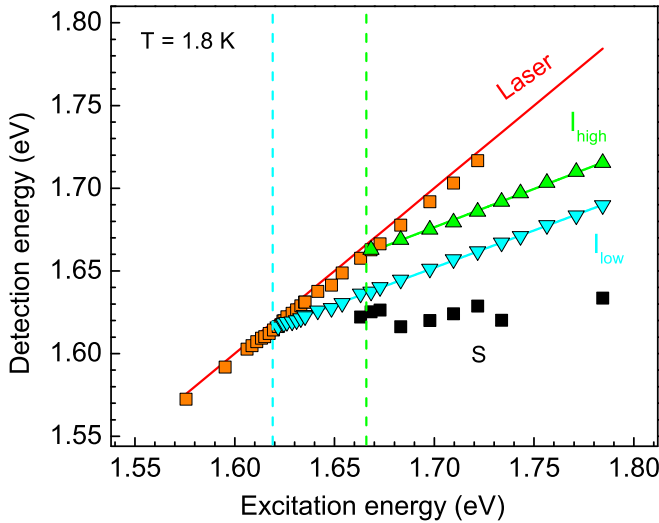


FIG. 4. Parameters of the PL lines resolved under selective excitation as a function of the excitation energy. $T = 1.8$ K. The shift of the laser is shown by the red line. Symbols give the energies of the PL lines corresponding to excitons in direct QDs (orange squares) and excitons in indirect QDs for the low-energy line (cyan triangles) and high-energy line (green triangles); the S line (black squares) does not move with varying laser energy. Crossing energies of the PL lines from direct and indirect QDs are $E_{\Gamma X}^{\text{low}} = 1.619$ eV and $E_{\Gamma X}^{\text{high}} = 1.666$ eV, as marked by the vertical dashed lines.

see that the ensemble has a bimodal distribution of QDs with $\Gamma - X$ transitions at energies $E_{\Gamma X}^{\text{low}} = 1.619$ eV and $E_{\Gamma X}^{\text{high}} = 1.666$ eV, shown in Fig. 4 by vertical dashed lines.

The vertical dashed lines in Figs. 3 and 4 shows the crossing energies of the PL lines from the direct and indirect exciton transitions which correspond to emission from QDs with equal energies of the Γ and X electron levels. The relatively broad line S , whose energy does not depend on the excitation energy, appears in the spectra at the low-energy $\Gamma - X$ intersection point. The origin of the S line is still unknown and is beyond the scope of this study. The PL polarization degree across the PL spectrum measured using optical orientation for excitation at $E_{\text{exc}} = 1.727$ eV is shown in Fig. 3 on the right axis. The PL in the low-energy spectral region, which corresponds to exciton recombination in direct band gap QDs (below $E_{\Gamma X}^{\text{low}}$), has practically no circular polarization due to breaking of the axial symmetry in the QDs, which results in a strong anisotropic electron-hole exchange interaction and mixing of the bright exciton states [20]. For indirect band gap QDs, the effect of the anisotropic electron-hole exchange interaction is negligible, and the pure exciton spin states $|\pm 1\rangle$ provide circularly polarized PL [12]. In zero magnetic field, the polarization degree for the indirect band gap QD emission is determined by three factors: (i) depolarization of the excitons caused by their scattering from the direct to the indirect state (since the photon absorption takes place via excited direct band gap QD states), i.e., by electron scattering from the Γ to the X valley before exciton recombination, (ii) exchange-induced depolarization due to $\Gamma - X$ mixing of the direct and indirect exciton states, and, finally, (iii) precession of the electron spin in the effective magnetic field of frozen fluctuations of the nuclear spins [12]. In this study we focus

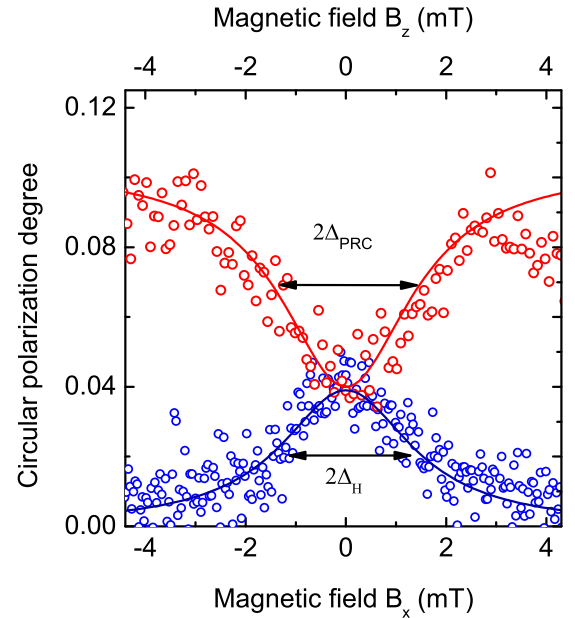


FIG. 5. Hanle curve and polarization recovery curve measured for the indirect QDs at 1.694 eV with excitation energy of 1.740 eV, $T = 4$ K.

on indirect QDs which are not affected by the $\Gamma - X$ mixing effect. As shown recently, these QDs emit at the I_{high} line in the PL spectra [12].

III. ELECTRON-NUCLEI INTERACTION IN THE X VALLEY

A. Experiment

For selective excitation ($E_{\text{exc}} = 1.740$ eV), the PL polarization degree in the I_{high} line at zero magnetic field is $\rho_c^0 \approx 0.04$. ρ_c^0 is determined by the ratio of the exciton spin relaxation time to its lifetime. The optical excitation of the QDs takes place quasiresonantly via excited direct band gap Γ states [see Fig. 2(a)]. The lifetime of the excited size-quantized states of direct excitons is short. As a result, the spin polarization of direct excitons has no time to change. Further depolarization of the excitons is caused by their scattering from the direct to the indirect states, i.e., by electron scattering from the Γ to the X valley before exciton recombination, as shown in Ref. [12].

Already in weak magnetic fields of a few milliteslas, $\rho_c(B)$ demonstrates strong changes (see Fig. 5). In Voigt geometry ($\mathbf{B} \perp z$) the Hanle effect is observed. The circular polarization degree is reduced down to zero with increasing field. The shape of the Hanle curve is well described by a Lorentzian, $\rho_c(B_x) = \rho_c^0 / (1 + B_x^2 / \Delta_H^2)$, with HWHM $\Delta_H = 1.25$ mT. In Faraday geometry ($\mathbf{B} \parallel z$), the circular polarization degree is gradually recovered with increasing magnetic field and saturates at a value ρ_{sat} that is approximately 2.5 times larger than ρ_c^0 . The shape of the PRC is also described by a Lorentz curve, $\rho_c(B_z) = \rho_c^0 + (\rho_{\text{sat}} - \rho_c^0) / (1 + \Delta_{\text{PRC}}^2 / B_z^2)$, with the same HWHM value as for the Hanle curve, $\Delta_{\text{PRC}} = 1.25$ mT.

The temperature dependence of Δ_H is shown in Fig. 6 by open black circles. One can see that Δ_H does not change with temperature up to $T = 30$ K. With a further increase of

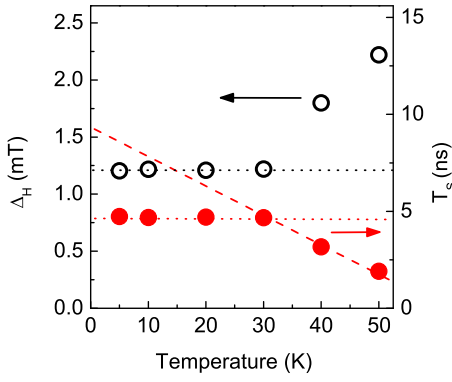


FIG. 6. Hanle curve half width (open black circles) and T_s calculated as $\hbar/(g\mu_B\Delta_H)$ (solid red circles) as functions of temperature. The dashed line is the linear extrapolation in the low-temperature region. Dotted lines are guides for the eye.

temperature, Δ_H increases linearly. Note that the relation $\Delta_{\text{PRC}} = \Delta_H$ holds throughout the studied temperature range. It is common practice to determine the spin lifetime T_s from the Hanle contour width by use of the equation $T_s = \hbar/(g\mu_B\Delta_H)$, where g is the electron g factor [11]. Taking into account that $g = 2$ [21,22] in these QDs, we calculated the dependence of $T_s(T)$, which is presented in Fig. 6. Theory [23] predicts a linear or a quadratic decrease of the spin lifetime with increasing temperature due to the increasing density of states involved in scattering. Actually, a linear decrease of $T_s(T)$ with increasing temperature occurs only above 30 K. Below 30 K, $T_s(T)$ is constant within the experimental accuracy. This unusual behavior suggests that at low temperatures Δ_H is limited by another factor. The only feasible candidate is the electron spin precession in the local magnetic fields created by the nuclear spin fluctuations [7,12], which can govern the electron spin dynamics in weak magnetic fields $B < \Delta_H$. This model will be considered in more detail in the next section.

In conclusion of this section, let us summarize the most important experimental findings: (i) The very weak anisotropic e-h exchange interaction and the quasiresonant excitation allow us to populate the X valley of indirect band gap QDs with spin-polarized electrons. (ii) At low temperatures, the relaxation of this spin polarization is determined by the hyperfine interaction with nuclear field fluctuations. This allows us to obtain the parameters of the hyperfine interaction from our experimental data.

B. Theory

In order to calculate the hyperfine coupling constants in the X valley of the conduction band of (In,Al)As the microscopic Hamiltonian of the hyperfine interaction has to be considered. Here, we derive the tensors of the hyperfine interaction with In, Al, and As atoms using the approach proposed by Gryncarova and Perel [24]. The general form of the hyperfine interaction Hamiltonian with the given nucleus is [25]

$$\mathcal{H}_{\text{hf}} = 2\mu_B\mu_I \mathbf{I} \left[\frac{8\pi}{3} \mathbf{s}\delta(\mathbf{r}) + \frac{\mathbf{I}}{r^3} - \frac{\mathbf{s}}{r^3} + 3\frac{\mathbf{r}(\mathbf{s}\mathbf{r})}{r^5} \right], \quad (1)$$

where \mathbf{I} is the nuclear spin; μ_B is the Bohr magneton; $\mu_I = g_I\mu_N$ is the magnetic moment of the nucleus, with g_I

being its g factor and μ_N being the nuclear magneton; \mathbf{s} is the electron spin; \mathbf{r} is the vector from the nucleus to the electron; and $\hbar\mathbf{l} = \mathbf{r} \times \mathbf{p}$ is the angular momentum, with \mathbf{p} being the linear momentum. The first term of the Hamiltonian describes the Fermi contact interaction, and the rest take into account the dipole-dipole interaction of the nuclear spin with orbital and spin magnetic moments of the electron.

In QDs the three equivalent X valleys are split due to size quantization, anisotropy of the QD shape, and strain. For this reason we neglect mixing of the valleys [26] and focus on the intravalley hyperfine interaction. The corresponding Hamiltonian was derived in the Supplemental Material of Ref. [10]. Below we briefly recapitulate the results.

The spin-orbit interaction in the conduction band of (In,Al)As is weak due to the large band gap at the X point [27,28], and therefore, the electron Bloch wave function is a product of a spinor and a real-valued orbital wave function. In the vicinities of a cation c and an anion a the latter can be decomposed in spherical harmonics. For the X_z valley oriented along the z axis the decomposition reads [10]

$$\Psi_c(\mathbf{r}) = \alpha_P \mathcal{P}_z(\mathbf{r}) + \alpha_T \mathcal{D}_{xy}(\mathbf{r}), \quad (2a)$$

$$\Psi_a(\mathbf{r}) = \alpha_S \mathcal{S}(\mathbf{r}) + \alpha_D \mathcal{D}_{z^2}(\mathbf{r}). \quad (2b)$$

Here, the functions $\mathcal{S}(\mathbf{r})$, $\mathcal{P}_i(\mathbf{r})$ ($i = x, y, z$), and $\mathcal{D}_i(\mathbf{r})$ ($i = xy, yz, xz, x^2 - y^2, z^2$) transform as the corresponding tesseral harmonics, and α_S , α_P , α_D , and α_T are real coefficients. This form of the wave functions can be derived from the symmetry analysis. It is important to note that the $\mathcal{S}(\mathbf{r})$ function can contribute to the electron wave function only in the vicinity of the As atoms. Indeed, the point symmetry group of the wave functions with the center of the transformations at the cation is Γ_7 (in the D_{2d} group) [10], which is inconsistent with the s type Bloch wave functions. The wave functions in the X_x and X_y valleys can be obtained from these expressions by symmetry transformations. We note that the hyperfine interaction is short range, so that the cross contributions to the Hamiltonian from orbitals of two different atoms are negligible [24].

In the X_z valley, the Hamiltonian of the hyperfine interaction of the localized electron can be written as

$$\mathcal{H}_{\text{hf}} = [A_\alpha^\perp (I_x s_x + I_y s_y) + A_\alpha^\parallel I_z s_z] |\psi(\mathbf{r}_i)|^2, \quad (3)$$

where A_α^\perp and A_α^\parallel are the constants of the hyperfine interaction with the nucleus at \mathbf{r}_i perpendicular and parallel to the valley and $\psi(\mathbf{r})$ is the localized electron envelop wave function. The index $\alpha = \text{Al, In, As}$ labels the different nuclear species, and we assume averaging over the two very similar isotopes of In. Note that all the nuclear isotopes in (In,Al)As have nonzero spin. The constants can be calculated using the Bloch wave functions (2) and the general Hamiltonian (1). For the calculation we use hydrogenlike functions with the orbital exponents calculated in Refs. [29,30]. We find

$$A_{\text{Al}}^\perp = (-0.4\alpha_p^2 + 0.1\alpha_t^2)A_0, \quad A_{\text{Al}}^\parallel = -2A_{\text{Al}}^\perp, \quad (4a)$$

$$A_{\text{In}}^\perp = (-0.7\alpha_p^2 + 1.6\alpha_t^2)A_0, \quad A_{\text{In}}^\parallel = -2A_{\text{In}}^\perp, \quad (4b)$$

$$A_{\text{As}}^\perp = (25.7\alpha_s^2 - 3.2\alpha_D^2 - 1.4\alpha_S\alpha_D)A_0, \quad (4c)$$

$$A_{\text{As}}^\parallel = (25.7\alpha_s^2 + 6.4\alpha_D^2 + 2.7\alpha_S\alpha_D)A_0, \quad (4d)$$

TABLE I. The values of the electron intravalley hyperfine coupling constants in the X and Γ valleys of $\text{In}_{0.7}\text{Al}_{0.3}\text{As}$ and in the Γ valley of GaAs with respect to $A_{\text{As}}^{\parallel}$ in $\text{In}_{0.7}\text{Al}_{0.3}\text{As}$.

	As	In	Al	Ga
$A_I^{\parallel}/A_{\text{As}}^{\parallel}$	1	0.032	0.023	
$A_I^{\perp}/A_{\text{As}}^{\parallel}$	0.61	-0.016	-0.012	
$A_I^{\Gamma}/A_{\text{As}}^{\parallel}$	1.6	1.2	0.44	
$A_I^{\Gamma}/A_{\text{As}}^{\parallel}$ (GaAs)	1.5			1.18

where A_0 is a constant [31]. Note that the term $\propto \alpha_S \alpha_D$ was omitted in Ref. [10]. The qualitatively different expressions for the hyperfine interaction constants with the cations and the anion are related to the different orbitals at these atoms, which contribute to the electron Bloch wave function [see Eq. (2)].

The coefficients of the decomposition in the orbital harmonics can be calculated for bulk InAs and AlAs crystals. We performed DFT calculations using the WIEN2K package [32] with the modified Becke-Johnson exchange-correlation potential [33] (we have checked that PBEsol generalized gradient approximation gives almost the same results). For AlAs we obtained $\alpha_P = 0.51$, $\alpha_T = -0.29$, $\alpha_S = 0.50$, and $\alpha_D = 0.63$. For InAs we obtained $\alpha_P = 0.69$, $\alpha_T = -0.35$, $\alpha_S = 0.49$, and $\alpha_D = 0.41$. The signs of these coefficients were found from additional tight-binding calculations.

For comparison, we perform similar calculations for the Γ valley of the conduction band. Here, the Bloch amplitude consists, by more than 98%, of s type functions, so the contributions of the other orbitals can be neglected, and the hyperfine interaction in the Γ valley is isotropic. As a result the wave function is described by the two amplitudes α_c and α_a of the S orbitals at the cation and anion, respectively. Using the hydrogenlike functions, as described above, we obtain the hyperfine coupling constants

$$A_{\text{Al}}^{\Gamma} = 9\alpha_{\text{Al}}^2 A_0, \quad A_{\text{In}}^{\Gamma} = 20.2\alpha_{\text{In}}^2 A_0, \quad A_{\text{As}}^{\Gamma} = 25.7\alpha_{\text{As}}^2 A_0. \quad (5)$$

These expressions are analogous to Eq. (4), and the constant A_0 here is the same. Further, the DFT calculations of the wave functions in the Γ valley of the conduction band of the bulk crystals yield the coefficients $\alpha_{\text{Al}} = 0.64$, $\alpha_{\text{As}} = 0.76$ for AlAs and $\alpha_{\text{In}} = 0.72$, $\alpha_{\text{As}} = 0.70$ for InAs.

Finally, we represent the alloy $\text{In}_{0.7}\text{Al}_{0.3}\text{As}$ as a mixture of InAs and AlAs with the corresponding weights. The relative values of the hyperfine coupling constants for the (In,Al)As and GaAs are given in Table I. Here, for the sake of convenience, we normalize all the constants by the $A_{\text{As}}^{\parallel}$ value of $\text{In}_{0.7}\text{Al}_{0.3}\text{As}$. In the X valley the hyperfine interaction is by far the strongest for the As nuclei, and for cations In and Al exchange coupling constants in the X valley are very small. This is due to the Fermi contact interaction of the s shell of the arsenic atom, which is stronger than the dipole-dipole interaction. The latter, however, results in an anisotropy of the hyperfine interaction, which is characterized by the parameter $\varepsilon = A_{\text{As}}^{\perp}/A_{\text{As}}^{\parallel} = 0.61$. In the Γ valley the hyperfine interaction is isotropic and stronger than in the X valley due to the completely s type of the Bloch amplitude.

The significant disadvantage of our approach is that it yields reliably only the relative values of the hyperfine cou-

TABLE II. Hyperfine constants for the X and Γ valleys of the $\text{In}_{0.7}\text{Al}_{0.3}\text{As}$ conduction band. The values are given in μeV .

	As	In	Al
A^{\parallel}	29	0.93	0.67
A^{\perp}	17.69	-0.46	-0.35
A^{Γ}	43.5 [35]	56 [37]	16 [38]

pling constants [10,34]. To find the absolute values, we performed a similar DFT calculation for bulk GaAs and obtained expressions similar to Eq. (5): $A_{\text{Ga}}^{\Gamma} = 9.88A_0$ and $A_{\text{As}}^{\Gamma} = 12.6A_0$. The relative values of these constants with respect to $A_{\text{As}}^{\parallel}$ in $\text{In}_{0.7}\text{Al}_{0.3}\text{As}$ are given in the last row in Table I. These constants were measured to be $A_{\text{Ga}}^{\Gamma} = 50 \mu\text{eV}$ and $A_{\text{As}}^{\Gamma} = 43.5 \mu\text{eV}$ [35,36]. The latter was measured with better precision, so we use it to find $A_0 = 3.5 \mu\text{eV}$. Note that this value corresponds to A_{Ga}^{Γ} in GaAs that is 7% larger than the one measured experimentally, and this can be considered an estimation of the accuracy of our approach.

With A_0 at hand, we calculate all the hyperfine coupling constants in $\text{In}_{0.7}\text{Al}_{0.3}\text{As}$ and collect the results in Table II. In particular, we find $A_{\text{As}}^{\perp} = \varepsilon A_{\text{As}}^{\parallel} = 17.69 \mu\text{eV}$, with $\varepsilon = 0.61$.

C. Modeling of experimentally measured Hanle and polarization recovery curves

The finite number of nuclear spins in a QD results in nuclear spin fluctuations. Their spin dynamics is very slow compared to the electron spin dynamics, and therefore, the nuclei effectively create the frozen Overhauser magnetic field, \mathbf{B}_N .

At low temperatures, as follows from Fig. 6, both the electron spin relaxation time and the exciton lifetime are much longer than the precession period of the electron spin in the effective field of the nuclear spin fluctuation. For this reason, only the component of the electron spin along the total field (external magnetic field plus effective Overhauser magnetic field) survives. By the time moment of recombination, the projection of the mean electron spin on the z axis equals

$$S_z = S_0 \langle \cos^2 \theta \rangle, \quad (6)$$

where $\mathbf{S}_0 \parallel z$ is the mean spin of the electrons just when they arrive at the X valley state, θ is the angle of the total field relative to the z axis, and the averaging is performed over the distribution function of nuclear spin fluctuations. Since the number of nuclear spins in the QD is large and they are, on average, unpolarized, the x , y , and z components of the hyperfine field are independent random variables characterized by a Gaussian distribution with the variance

$$\langle (B_N^{\alpha})^2 \rangle = \frac{I(I+1)V_0}{3V} \left(\frac{A_{\text{As}}^{\alpha}}{g_e \mu_B} \right)^2 = \Delta_{\alpha}^2 B_N^2, \quad (7)$$

i.e., mean-square hyperfine field created by one nucleus multiplied by the number of nuclei in the QD. Here, $\alpha \in \{x, y, z\}$, $V_0 = 45.1 \times 10^{-24} \text{ cm}^3$ is the primitive cell volume, V is the QD volume, and $I = 3/2$, with g_e being the electron g factor in the X valley. We neglected here the hyperfine interaction

with the cations. Here, $\Delta_\alpha = A_{As}^\alpha/A_{As}^\parallel$, and

$$B_N = \frac{A_{As}^\parallel}{g_e \mu_B} \sqrt{\frac{I(I+1)V_0}{3V}} \quad (8)$$

is the rms nuclear fluctuation field along the axis of the X valley.

The square cosine of the inclination angle of the total field $\mathbf{B}^* = \mathbf{B} + \mathbf{B}_N$ equals

$$\cos^2 \theta = \frac{B_z^{*2}}{B_x^{*2} + B_y^{*2} + B_z^{*2}} = \frac{b_z^2}{b_x^2 + b_y^2 + b_z^2}, \quad (9)$$

where $\mathbf{b} \equiv \mathbf{B}^*/B_N$. By averaging Eq. (6) over the Gaussian distribution of nuclear fluctuation field we obtain an expression for S_z :

$$S_z(B/B_N) = \frac{S_0}{\sqrt{8\pi^3 \Delta_x \Delta_y \Delta_z}} \iiint \frac{b_z^2}{b_x^2 + b_y^2 + b_z^2} \exp \left[-\frac{b_x^2}{2\Delta_x^2} - \frac{b_y^2}{2\Delta_y^2} - \frac{(b_z - B/B_N)^2}{2\Delta_z^2} \right] db_x db_y db_z \quad (10)$$

in the case of the PRC, and

$$S_z(B/B_N) = \frac{S_0}{\sqrt{8\pi^3 \Delta_x \Delta_y \Delta_z}} \iiint \frac{b_z^2}{b_x^2 + b_y^2 + b_z^2} \exp \left[-\frac{(b_x - B/B_N)^2}{2\Delta_x^2} - \frac{b_y^2}{2\Delta_y^2} - \frac{b_z^2}{2\Delta_z^2} \right] db_x db_y db_z \quad (11)$$

in the case of the Hanle effect.

The numeric solution of the integrals in Eqs. (10) and (11) yields S_z/S_0 as a function of B/B_N . For a given anisotropy of the hyperfine interaction and orientation of the magnetic field, the curves can be fitted to the experimentally measured Hanle and polarization recovery curves by changing the single parameter B_N .

In Figure 7 the experimental curves are shown along with the fits by the numerical solution of the integrals in Eqs. (10) and (11) for the cases when the axis of the X valley is directed along the structural axis z [Fig. 7(a)], along x [Fig. 7(b)], and along y [Fig. 7(c)] and for mixing of the x and y directions [Fig. 7(d)]. The mixing of x and y means that the electron rapidly hops between the X_x and X_y valleys. This hopping can lead to the spin relaxation; thus, we implicitly assume that the hopping time is shorter than $\hbar^2/(g_e^2 \mu_B^2 B_N^2 \tau_0)$, where τ_0 is the exciton lifetime.

One can see that full agreement between both experimentally measured curves and theoretical calculations is obtained only when the X valley axis is directed along the z direction. However, for all four variants of the X valley directions the Hanle curves are well fitted assuming $B_N = 1.25$ mT.

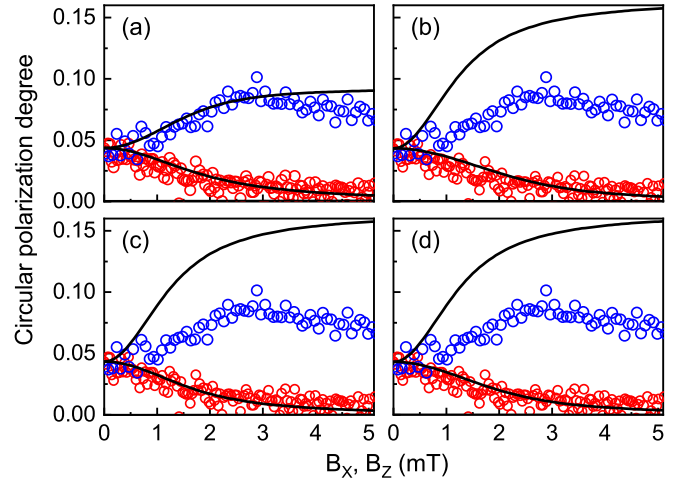


FIG. 7. Experimental Hanle (red circles) and PRC (blue circles) curves measured at $T = 4$ K fitted with Eqs. (10) and (11) (lines) for the cases when the X valley is directed along (a) the z axis $\Delta_x = \Delta_y = 0.61$, $\Delta_z = 1$; (b) the x axis $\Delta_x = 1$, $\Delta_y = \Delta_z = 0.61$; (c) the y axis $\Delta_x = \Delta_z = 0.61$, $\Delta_y = 1$; and (d) the x axis and y axis with equal probabilities with rapid electron transitions between the two valleys (xy mixing) $\Delta_x = \Delta_y = 0.805$, $\Delta_z = 0.61$.

As we mentioned above, the hyperfine interaction in the X valley is the strongest for the As nuclei and negligibly small for the In and Al nuclei. Using $B_N = 1.25$ mT, we can find from Eq. (8) the constant A_{As}^\parallel for the given QD volume. Since we do not know the volume exactly, we plot in Fig. 8 A_{As}^\parallel as a function of the QD volume V .

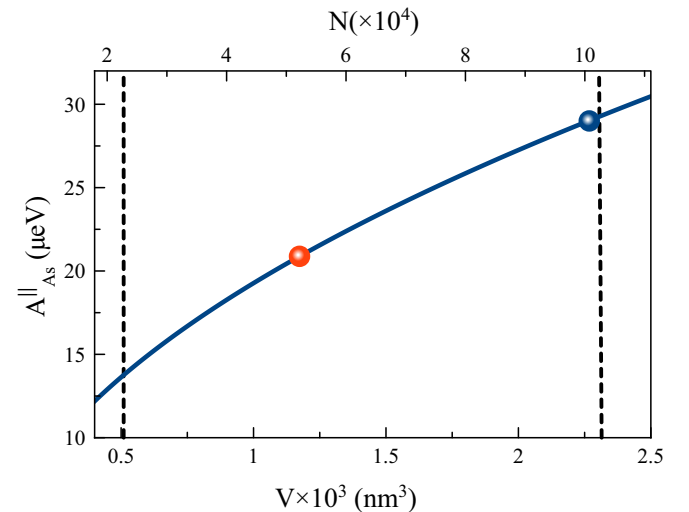


FIG. 8. The hyperfine constant in the X valley for As as a function of QD volume (blue curve). The red point corresponds to V_{av} ; the blue point is the theoretically calculated hyperfine constant of A_{As}^\parallel . Dashed lines show the limits of the QD volumes. The numbers of nuclei in the QD corresponding to QD volume are given on the top axis.

The two dashed lines in Fig. 8 show the margins for the QD volume found from the TEM measurements [$V = (0.5 - 2.3) \times 10^3 \text{ nm}^3$] and the corresponding margins for the hyperfine coupling constant: $A_{\text{As}}^{\parallel} = 13.7\text{--}29.3 \mu\text{eV}$. The average QD volume is $V_{av} = 1.18 \times 10^3 \text{ nm}^3$, which corresponds to $A_{\text{As}}^{\parallel} = 20.3 \mu\text{eV}$ (red dot). The theoretical value $A_{\text{As}}^{\parallel} = 29 \mu\text{eV}$ lies within the margins. Note that the number of nuclei in the QD $N = 2V_{av}/V_0 = 5 \times 10^4$ is large, which justifies our effective mass and mean-field approximations. The obtained estimations for the hyperfine coupling constants in Table II are the main result of the present study.

IV. DISCUSSION AND CONCLUSIONS

In our description of the PL polarization we assumed that it equals the electron spin polarization. Thus, we neglected the hole spin polarization. Indeed, if the polarization of the PL were determined by the hole spin, it would be independent of the transverse magnetic field because of the negligible heavy-hole transverse g factor. In our experiments, by contrast, the polarization degree is equally sensitive to the longitudinal and transverse magnetic fields, $\Delta_H = \Delta_{\text{PRC}}$ (see Fig. 5). This indicates that the polarization of the PL is indeed determined by the electron spin polarization. We note also that we neglected the electron-hole exchange interaction, which is known to be weak for the indirect band gap (In,Al)As QDs [12].

From Fig. 7 it is seen that the best agreement of the theoretical calculations with the experimental data is observed when the X valley is directed along the z axis. This is surprising since it is believed that this valley is pushed up from the two X_x and X_y valleys. One possible explanation is that it is the z -oriented X valley that is populated by the electron transfer from the Γ minimum under the excitation conditions used in our experiments. Another explanation is that it is an effect of the electron-hole exchange interaction, which might be not as weak as generally believed. Indeed, the exchange interaction effectively acts as a magnetic field along the z axis and increases the electron spin polarization in zero field relative to its value in strong longitudinal magnetic field. The detailed analysis of the total intensity of the PL can help to clarify this issue in future works. In any case, fitting the experimental curves with models assuming that the X valley is directed along x , y , or both axes shows good agreement for

the Hanle curves and gives the same value of $B_N = 1.25 \text{ mT}$. This fact allows us to calculate the hyperfine constants for the As, In, and Al nuclei in the X valley. From Table II it is seen that only the As nuclei have a strong interaction with the electron spin in the X valley. This fact results in a considerable narrowing of the Hanle curve compared to that of Γ excitons, in spite of the modest difference in As hyperfine constants for the X and Γ points. The width of the Hanle curve is further narrowed due to the relatively large g factor in the X valley.

In conclusion, experiments on the optical spin orientation of indirect excitons formed by Γ valley holes and X valley electrons in (In,Al)As/AlAs QDs reveal magnetic field dependences of the PL polarization that are typical of electrons interacting with nuclear spin fluctuations. With the knowledge of the electron g factor in the X valley, $g \approx 2$, the measured magnetic field scales of the polarization suppression in the transverse magnetic field (Hanle effect) and its recovery in the longitudinal field give an estimate of the strength of the hyperfine interaction of the X valley electron with all the nuclear spins in the quantum dot. The comparison with theory based on symmetry considerations and DFT calculations yields the values of the hyperfine constants for each of the three nuclear species (As, In, and Al) present in the structure.

ACKNOWLEDGMENTS

We are grateful to M.O. Nestoklon for fruitful discussions. This work was supported by the Deutsche Forschungsgemeinschaft via Project No. 409810106 and by the Russian Foundation for Basic Research Grant No. 19-52-12001. On the German side, the support in the frame of the ICRC TRR 160 by the Deutsche Forschungsgemeinschaft is also acknowledged (Projects No. A4, No. A6, and No. B2), to which the Russian Foundation for Basic Research also contributes (Grants No. 19-52-12038 and No. 19-52-12043). M.S.K. and K.V.K. acknowledge Saint-Petersburg State University for a research grant, Grant No. 51125686. D.S.S. was partially supported by the RF President Grant No. MK-1576.2019.2, the Basis Foundation, and the Russian Foundation for Basic Research (Grants No. 17-02-0383 and No. 19-52-12054). T.S.S. acknowledges the financial support by the Russian Foundation for Basic Research (Grant No. 19-02-00098) and by Act 211 of the Government of the Russian Federation (Contract No. 02.A03.21.0006).

[1] S. D. Bader and S. S. P. Parkin, Spintronics, *Annu. Rev. Condens. Matter Phys.* **1**, 71 (2010).
 [2] N. Somaschi, V. Giesz, L. De Santis, J. C. Loredó, M. P. Almeida, G. Hornecker, S. L. Portalupi, T. Grange, C. Anton, J. Demory, C. Gomez, I. Sagnes, N. D. Lanzillotti-Kimura, A. Lemaitre, A. Auffeves, A. G. White, L. Lanco, and P. Senellart, Near-optimal single-photon sources in the solid state, *Nat. Photonics* **10**, 340 (2016).
 [3] W. B. Gao, A. Imamoglu, H. Bernien, and R. Hanson, Coherent manipulation, measurement and entanglement of individual solid-state spins using optical fields, *Nat. Photonics* **9**, 363 (2015).

[4] J. H. Smet, R. A. Deutschmann, F. Ertl, W. Wegscheider, G. Abstreiter, and K. von Klitzing, Gate-voltage control of spin interactions between electrons and nuclei in a semiconductor, *Nature (London)* **415**, 281 (2002).
 [5] E. A. Chekhovich, M. N. Makhonin, A. I. Tartakovskii, A. Yacoby, H. Bluhm, K. C. Nowack, and L. M. K. Vandersypen, Nuclear spin effects in semiconductor quantum dots, *Nat. Mater.* **12**, 494 (2013).
 [6] B. Urbaszek, X. Marie, T. Amand, O. Krebs, P. Voisin, P. Maletinsky, A. Högele, and A. Imamoglu, Nuclear spin physics in quantum dots: An optical investigation, *Rev. Mod. Phys.* **85**, 79 (2013).

- [7] I. A. Merkulov, Al. L. Efros, and M. Rosen, Electron spin relaxation by nuclei in semiconductor quantum dots, *Phys. Rev. B* **65**, 205309 (2002).
- [8] J. Fischer, W. A. Coish, D. V. Bulaev, and D. Loss, Spin decoherence of a heavy hole coupled to nuclear spins in a quantum dot, *Phys. Rev. B* **78**, 155329 (2008).
- [9] T. S. Shamirzaev, Exciton recombination and spin dynamics in indirect-gap quantum wells and quantum dots, *Phys. Solid State* **60**, 1554 (2018).
- [10] A. V. Shchepetilnikov, D. D. Frolov, Yu. A. Nefyodov, I. V. Kukushkin, D. S. Smirnov, L. Tiemann, C. Reichl, W. Dietsche, and W. Wegscheider, Nuclear magnetic resonance and nuclear spin relaxation in AlAs quantum well probed by ESR, *Phys. Rev. B* **94**, 241302(R) (2016).
- [11] I. A. Merkulov and V. G. Fleisher, Optical orientation of coupled electron-nuclear spin system of a semiconductor, in *Optical Orientation*, edited by F. Meier and B. P. Zakharchenya (Elsevier Science Publishers B.V., Amsterdam, 1984), Chap. 5, p. 173.
- [12] J. Rautert, T. S. Shamirzaev, S. V. Nekrasov, D. R. Yakovlev, P. Klenovsky, Yu. G. Kusrayev, and M. Bayer, Optical orientation and alignment of excitons in direct and indirect band gap (In, Al)As/AlAs quantum dots with type-I band alignment, *Phys. Rev. B* **99**, 195411 (2019).
- [13] T. S. Shamirzaev, A. V. Nenashev, A. K. Gutakovskii, A. K. Kalagin, and K. S. Zhuravlev, Atomic and energy structure of InAs/AlAs quantum dots, *Phys. Rev. B* **78**, 085323 (2008).
- [14] T. S. Shamirzaev, A. V. Nenashev, and K. S. Zhuravlev, Coexistence of direct and indirect band structures in arrays of InAs/AlAs quantum dots, *Appl. Phys. Lett.* **92**, 213101 (2008).
- [15] J.-W. Luo, A. Franceschetti, and A. Zunger, Quantum-size-induced electronic transitions in quantum dots: Indirect band-gap GaAs, *Phys. Rev. B* **78**, 035306 (2008).
- [16] I. Vurgaftman, J. R. Meyer, and L. R. Ram-Mohan, Band parameters for III-V compound semiconductors and their alloys, *J. Appl. Phys.* **89**, 5815 (2001).
- [17] T. S. Shamirzaev, J. Debus, D. S. Abramkin, D. Dunker, D. R. Yakovlev, D. V. Dmitriev, A. K. Gutakovskii, L. S. Braginsky, K. S. Zhuravlev, and M. Bayer, Exciton recombination dynamics in an ensemble of (In, Al)As/AlAs quantum dots with indirect band-gap and type-I band alignment, *Phys. Rev. B* **84**, 155318 (2011).
- [18] T. S. Shamirzaev, J. Debus, D. R. Yakovlev, M. M. Glazov, E. L. Ivchenko, and M. Bayer, Dynamics of exciton recombination in strong magnetic fields in ultrathin GaAs/AlAs quantum wells with indirect band gap and type-II band alignment, *Phys. Rev. B* **94**, 045411 (2016).
- [19] T. S. Shamirzaev, D. S. Abramkin, A. V. Nenashev, K. S. Zhuravlev, F. Trojanek, B. Dzurak and P. Maly, Carrier dynamics in InAs/AlAs quantum dots: Lack in carrier transfer from wetting layer to quantum dots, *Nanotechnology* **21**, 155703 (2010).
- [20] M. Bayer, G. Ortner, O. Stern, A. Kuther, A. A. Gorbunov, A. Forchel, P. Hawrylak, S. Fafard, K. Hinzer, T. L. Reinecke, S. N. Walck, J. P. Reithmaier, F. Klopff, and F. Schäfer, Fine structure of neutral and charged excitons in self-assembled In(Ga)As/(Al)GaAs quantum dots, *Phys. Rev. B* **65**, 195315 (2002).
- [21] J. Debus, T. S. Shamirzaev, D. Dunker, V. F. Sapega, E. L. Ivchenko, D. R. Yakovlev, A. I. Toropov, and M. Bayer, Spin-flip Raman scattering of the $\Gamma - X$ mixed exciton in indirect band gap (In, Al)As/AlAs quantum dots, *Phys. Rev. B* **90**, 125431 (2014).
- [22] V. Yu. Ivanov, T. S. Shamirzaev, D. R. Yakovlev, A. K. Gutakovskii, Ł. Owczarczyk, and M. Bayer, Optically detected magnetic resonance of photoexcited electrons in (In, Al)As/AlAs quantum dots with indirect band gap and type-I band alignment, *Phys. Rev. B* **97**, 245306 (2018).
- [23] M. W. Wu, J. H. Jiang, and M. Q. Weng, Spin dynamics in semiconductors, *Phys. Rep.* **493**, 61 (2010).
- [24] E. I. Gryncharova and V. I. Perel, Relaxation of nuclear spins interacting with holes in semiconductors, *Sov. Phys. Semicond.* **11**, 997 (1977).
- [25] A. Abragam, *The Principles of Nuclear Magnetism* (Oxford University Press, Oxford, 1961).
- [26] I. D. Avdeev and D. S. Smirnov, Hyperfine interaction in atomically thin transition metal dichalcogenides, *Nanoscale Adv.* **1**, 2624 (2019).
- [27] I. A. Yugova, A. Greilich, D. R. Yakovlev, A. A. Kiselev, M. Bayer, V. V. Petrov, Yu. K. Dolgikh, D. Reuter, and A. D. Wieck, Universal behavior of the electron g factor in GaAs/Al_xGa_{1-x}As quantum wells, *Phys. Rev. B* **75**, 245302 (2007).
- [28] E. L. Ivchenko, *Optical Spectroscopy of Semiconductor Nanostructures* (Alpha Science, Harrow, UK, 2005).
- [29] E. T. Clementi and D. L. Raimondi, Atomic screening constants from SCF functions, *J. Chem. Phys.* **38**, 2686 (1963).
- [30] E. Clementi, D. L. Raimondi, and W. P. Reinhardt, Atomic screening constants from SCF functions. II. Atoms with 37 to 86 electrons, *J. Chem. Phys.* **47**, 1300 (1967).
- [31] We neglect here the difference between the magnetic moments of ¹¹³In and ¹¹⁵In.
- [32] P. Blaha, K. Schwarz, G. Madsen, D. Kvaniscka, and J. Luitz, *WIEN2K, an Augmented Plane Wave Plus Local Orbitals Program for Calculating Crystal Properties* (Vienna University of Technology, Vienna, 2001).
- [33] F. Tran and P. Blaha, Accurate Band Gaps of Semiconductors and Insulators with a Semilocal Exchange-Correlation Potential, *Phys. Rev. Lett.* **102**, 226401 (2009).
- [34] E. A. Chekhovich, M. M. Glazov, A. B. Krysa, M. Hopkinson, P. Senellart, A. Lemaitre, M. S. Skolnick, and A. I. Tartakovskii, Element-sensitive measurement of the hole-nuclear spin interaction in quantum dots, *Nat. Phys.* **9**, 74 (2013).
- [35] E. A. Chekhovich, A. Ulhaq, E. Zallo, F. Ding, O. G. Schmidt, and M. S. Skolnick, Measurement of the spin temperature of optically cooled nuclei and GaAs hyperfine constants in GaAs/AlGaAs quantum dots, *Nat. Mater.* **16**, 982 (2017).
- [36] D. Paget, G. Lampel, B. Sapoval, and V. I. Safarov, Low field electron-nuclear spin coupling in gallium arsenide under optical pumping conditions, *Phys. Rev. B* **15**, 5780 (1977).
- [37] P. F. Braun, B. Urbaszek, T. Amand, X. Marie, O. Krebs, B. Eble, A. Lemaitre, and P. Voisin, Bistability of the nuclear polarization created through optical pumping in In_{1-x}Ga_xAs quantum dots, *Phys. Rev. B* **74**, 245306 (2006).
- [38] J. R. Morton and K. F. Preston, Atomic parameters for paramagnetic resonance data, *J. Magn. Reson.* **30**, 577 (1978).